



# The transition from re-entrant flow-driven to shockwave-driven cloud cavitation

Grigorios Hatzissawidis<sup>1</sup>, Maximilian M.G. Kuhr<sup>1</sup> and Peter F. Pelz<sup>1,†</sup>

<sup>1</sup>Chair of Fluid Systems, Technische Universität Darmstadt, Otto-Berndt-Str. 2, 64287 Darmstadt, Germany

(Received 27 May 2024; revised 25 October 2024; accepted 12 December 2024)

Understanding the mechanism of hydrodynamic cloud cavitation is crucial to reducing noise, vibration and wear. Recent studies have clarified the physics of two distinct formation mechanisms of cloud cavitation. Ganesh *et al.* (*J. Fluid Mech.*, vol. 802, 2016, pp. 37–78) identified the propagation of bubbly shockwaves as a cloud detachment mechanism. Pelz *et al.* (*J. Fluid Mech.*, vol. 817, 2017, pp. 439–454) explained the influence of Reynolds number and cavitation number on asymptotic growth of the cavity sheet and its periodic shedding caused by re-entrant flow. In this paper the two mechanisms are set in relation to each other. For this, we show firstly that the transition from re-entrant flow to shockwave-driven cloud cavitation is given by a kinematic condition, namely the asymptotic sheet length equates to the chord length,  $\hat{a} = L$ . For  $\hat{a} > L$  shockwave-driven cloud cavitation dominates. For  $\hat{a} < L$  re-entrant flow-driven cloud cavitation dominates. As the cavitation number decreases, the closure region of the cavity sheet reaches the trailing edge of the hydrofoil, identifying the trailing edge as a trigger for condensation shockwaves, particularly as re-entrant flow-driven cavitation diminishes. Since the sheet length is an implicit function of the cavitation number, the kinematic condition  $\hat{a}/L = 1$  results in a critical cavitation number  $\sigma_{II,III}$  that is calculated analytically and validated by experiments. Secondly, we derive the relationship between the Strouhal number and the asymptotic sheet length for re-entrant flow-driven cloud cavitation. The model presented here is thoroughly validated by experiments.

**Key words:** multiphase flow, cavitation, bubble dynamics

## 1. Introduction

Cloud cavitation is among the most severe manifestations of cavitation, specifically concerning its potential to cause damage. It refers to the periodic detachment and advection of large-scale cavitation vortices, observed in pumps, ship propellers, nozzles,

† Email address for correspondence: [peter.pelz@fst.tu-darmstadt.de](mailto:peter.pelz@fst.tu-darmstadt.de)

etc. associated with unsteadiness leading to noise and potentially to vibration, efficiency drop and erosion.

Cloud cavitation has four phases: (i) nucleation near the leading edge of the hydrofoil, (ii) asymptotic sheet growth to a sheet length  $\hat{a}$ , (iii) detachment of cavitation clouds, i.e. bubbly vortices, and advection due to the bulk flow, and (iv) cloud collapse.

Over many years, the re-entrant flow – a thin and viscous liquid film flow developing at the cavity closure region, which flows beneath the cavity sheet – was believed to be the sole mechanism driving cloud cavitation: Knapp (1955) firstly reported periodic cloud cavitation due to the re-entrant flow, followed by many notable studies (Furness & Hutton 1975; Lush & Skipp 1986; Le, Franc & Michel 1993; De Lange & De Bruin 1998; Pham, Larrarte & Fruman 1999; De Graaf, Brandner & Pearce 2017; Pelz, Keil & Groß 2017; Smith *et al.* 2020). Kawanami *et al.* (1997) demonstrated in their experiments on the flow around a hydrofoil the existence of the re-entrant flow using dye injections as well as an obstacle to hinder the re-entrant flow reaching the leading edge, suppressing cloud cavitation. Callenaere *et al.* (2001) reported that the development of the re-entrant flow depends on the adverse pressure gradient and the thickness relation between the cavity and the re-entrant flow. Re-entrant flow-driven cloud cavitation occurs when the re-entrant flow reaches the cavity leading edge and breaks through the cavity sheet. The fundamental cloud shedding frequency associated with the re-entrant flow is known to decrease with decreasing cavitation number for otherwise constant flow conditions (Arndt *et al.* 2000; Kjeldsen, Arndt & Effertz 2000; Dular & Bachert 2009; Smith *et al.* 2020; Hatzissawidis, Ludwig & Pelz 2021). This happens because the asymptotic sheet length becomes larger; as a result, the sheet takes more time to develop, and the re-entrant flow needs to travel a longer distance. The asymptotic sheet length, as introduced by Pelz *et al.* (2017), refers to the theoretical sheet length that would be reached over infinite time, i.e. as  $t \rightarrow \infty$ ,  $a(t) \rightarrow \hat{a}$ .

Apart from the re-entrant flow, there is a second mechanism for cloud cavitation at low cavitation number, namely the propagation of shockwaves. Shockwaves in bubbly flows are associated with a severe drop in the speed of sound of a liquid–gas bubbly mixture. Reisman, Wang & Brennen (1998) laid the groundwork for recognising the critical role of shockwaves in cloud cavitation, although they had been posited decades earlier by Jakobsen (1964).

Ganesh, Makiharju & Ceccio (2016) firstly described in detail shockwave-driven cloud cavitation in a nozzle with a wedge geometry using X-ray densitometry and high-speed visualisation. They associated the transition from re-entrant flow-driven cavitation to shockwave-driven cavitation with a critical Mach number. This investigation initiated experimental (Wu, Maheux & Chahine 2017; Jahangir, Hogendoorn & Poelma 2018; Wu, Ganesh & Ceccio 2019) as well as numerical studies (Budich, Schmidt & Adams 2018; Trummler, Schmidt & Adams 2020) regarding shockwaves in cloud cavitation.

The transition between the two regimes, which manifests as an abrupt change in the dynamics between a high-frequency and low-frequency shedding, was identified by Arndt *et al.* (2000) and Kjeldsen *et al.* (2000) for the flow around a NACA 0015 hydrofoil, and has also been reported by Leroux, Coutier-Delgosha & Astolfi (2005) and recently by Jahangir *et al.* (2018), Smith *et al.* (2020) and Bhatt, Ganesh & Ceccio (2023). The high-frequency shedding was associated with the re-entrant flow, the low-frequency with shockwaves, as first reported by Arndt *et al.* (2000).

Recent and insightful experimental studies about a NACA 0015 hydrofoil conducted by Bhatt *et al.* (2023) are consistent with the findings in this study. They have revealed a smooth transition, wherein re-entrant flow and shockwaves manifest with a specific

## The transition to shockwave-driven cloud cavitation

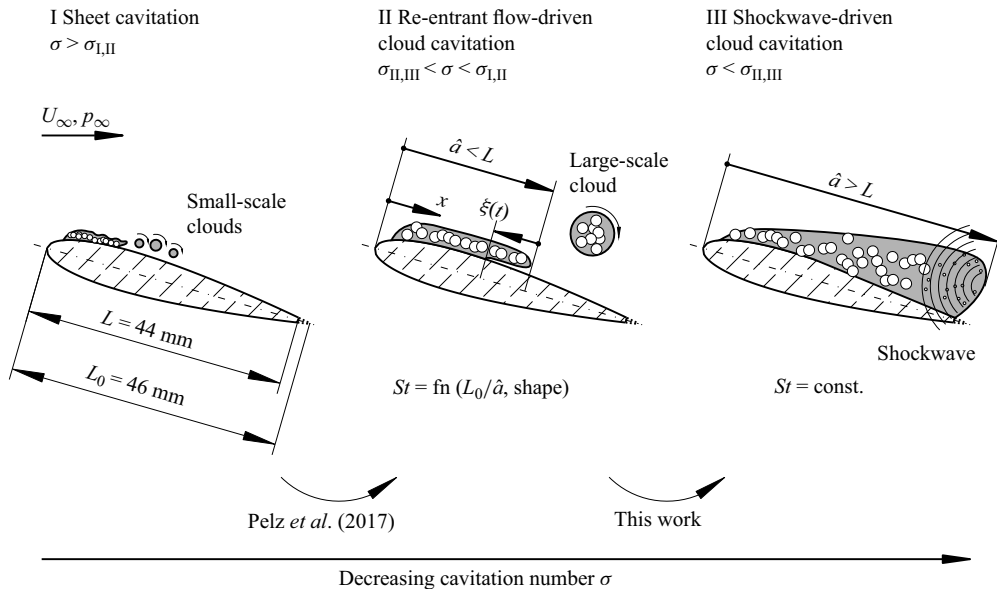


Figure 1. Schematic overview of the three cloud shedding mechanisms: I sheet cavitation, II re-entrant flow driven and III shockwave driven.

probability expressed as a likelihood function over the cavitation number. At lower cavitation numbers, there is an increased probability of the occurrence of shockwaves.

Despite recent experimental and numerical activities, there is still a lack of knowledge regarding the transition from re-entrant flow-driven cavitation to shockwave-driven cavitation. The primary question addressed in the current study is: What is the condition that causes the transition from shockwave-driven to re-entrant flow-driven cloud cavitation for lifting surfaces? Our hypothesis is that the transition occurs if  $\hat{a} = L$ , i.e. when the closure region of the cavity sheet hits the hydrofoil's trailing edge of chord length  $L$ .

To address this question and to validate the hypothesis, we first draw a rough picture in § 2 for the transition mechanisms and dynamics about a hydrofoil. By using the condition  $\hat{a}/L = 1$ , we identify a critical cavitation number, where the transition from re-entrant flow-driven cloud cavitation to shockwave-driven cloud cavitation occurs, § 2.1. We further predict the Strouhal number for the re-entrant flow-driven cloud cavitation from the sheet velocity and re-entrant flow dynamics described by a second-order nonlinear ordinary differential equation in § 2.2. After deriving the physical models, we introduce the experimental set-up in § 3 and conduct an experimental validation in § 4. The conclusions are summarised in § 5.

## 2. Cloud cavitation dynamics and physical modelling

A schematic representation delineating the mechanisms of shedding and transition is illustrated in figure 1. The transition from sheet cavitation, regime I, to re-entrant flow-driven cloud cavitation, regime II, is examined by Pelz *et al.* (2017). The present study deals with the transition from regime II to shockwave-driven cloud cavitation, regime III.

In this study, we consider the flow about a hydrofoil. The velocity and static pressure at infinity are denoted by  $U_\infty$  and  $p_\infty$ , respectively. The operation point is given by the cavitation number,  $\sigma := 2(p_\infty - p_v)/\rho U_\infty^2$ , where  $p_v$  is the vapour pressure and  $\rho$  is the

density of water, and the Reynolds number,  $Re := U_\infty L_0 / \nu$ , where  $\nu$  is the kinematic viscosity of water. The shape of the hydrofoil, i.e. NACA 0015 and the incidence  $\alpha$ , give the pressure distribution along the suction side for the non-cavitating hydrofoil  $c_p(x/L_0) := 2(p(x/L_0) - p_\infty) / \rho U_\infty^2$  with  $p(x/L_0)$  being the static pressure along the hydrofoil's surface. We distinguish between the nominal  $L_0$  and the real chord length  $L$ ,  $L < L_0$ , due to manufacturing reasons regarding the trailing edge as usual, cf. [figure 1](#). We experience the different cavitation regimes as the static pressure  $p_\infty$  and hence the cavitation number  $\sigma$  at constant Reynolds number is reduced. At high cavitation numbers, a cavitation sheet is formed. This sheet is attached to a line near the leading edge, and is quasi-steady in the time average. It initiates as microscopic patches close to the leading edge and evolves into a macroscopic sheet, where small-scale horseshoe vortices are shed due to interfacial instabilities, cf. Brandner *et al.* (2010). This regime I is known as sheet cavitation. A further reduction of the cavitation number, leading to the surpassing of the critical value  $\sigma_{I,II}$ , results in a well-defined periodic cloud shedding. This regime II is known as re-entrant flow-driven cloud cavitation with  $\hat{a} < L_0$ . Pelz *et al.* (2017) showed that  $\sigma_{I,II}$  is a function of Reynolds number and surface roughness.

From the point of view of dimensional analysis, the asymptotic sheet length  $\hat{a}$  is a function of the cavitation number  $\sigma$ , the dimensionless nucleation rate  $f_0 R_0 / U_0$  ( $f_0$ ,  $R_0$  and  $U_0$  are the nucleation rate, the initial bubble size at the cavity leading edge and the fluid velocity at the cavity interface,  $U_0 = U_\infty \sqrt{1 + \sigma}$ , respectively), and the shape that encompasses all dimensionless length scales of the body, i.e.  $\text{shape} = \{\alpha, \text{NACA0015}\}$ , fully considered by  $c_p(x/L_0)$ . Hence, the dimensional analysis yields  $\hat{a}/L_0 = \text{fn}(\sigma, f_0 R_0 / U_0, \text{shape})$  or implicitly  $0 = \text{Fn}(\sigma, f_0 R_0 / U_0, c_p(\hat{a}/L_0))$ . The abbreviations  $\text{fn}$  and  $\text{Fn}$  are arbitrary explicit and implicit functions, respectively. Aligning with this, Pelz *et al.* (2017) derived the implicit expression of the asymptotic sheet length as

$$c_p(\hat{a}/L) \approx 1.67 \left( \frac{f_0 R_0}{U_0} \right)^2 - \sigma. \tag{2.1}$$

This simple model is not only valid for a nozzle but also for flow about lifting surfaces such as the NACA 0015 hydrofoil, as the comparison with the experimental data in this work shows, cf. [figure 2\(b\)](#). As this paper further shows, the model also provides access to the critical cavitation number, which characterises the transition from regime II to III, cf. § 2.1.

The large kinematic scales in regime II are the cloud shedding frequency  $f$ , and the sheet length  $\hat{a}$ . Assuming that the frequency  $f$  is an explicit function of the dependent variable  $\hat{a}$  and only implicitly dependent on the independent variables  $\sigma$ ,  $f_0 R_0 / U_0$  and  $U_\infty$ , as well as the shape of the hydrofoil, we obtain  $St := f L_0 / U_\infty = \text{fn}(L_0 / \hat{a}, \text{shape})$ . The first term of a Taylor expansion of this relation yields  $St \approx L_0 / \hat{a} C(\text{shape})$ , where  $C$  is only a function of the body's shape. In fact this relation has been well validated by our experiments, see [figure 2\(a,c\)](#), and those of others, cf. § 1.

Regime III or shockwave-driven cloud cavitation occurs when the cavitation number  $\sigma$  is lowered further: the sheet reaches the trailing edge,  $\hat{a}/L = 1$ , and a shockwave is initiated, [figure 1](#). It should be mentioned that in regime III a re-entrant flow may also contribute to a premature cloud shedding, although the main shedding cycle is driven by a shockwave (Budich *et al.* 2018; Venning, Pearce & Brandner 2022; Zhang *et al.* 2022). Furthermore, an advecting cloud from the previous cycle may influence the sheet growth or initiate a shockwave leading to an extinction of the growing cavity sheet, cf. Bhatt *et al.* (2023). However, the primary mechanism for the transition from regime II to III is

## The transition to shockwave-driven cloud cavitation

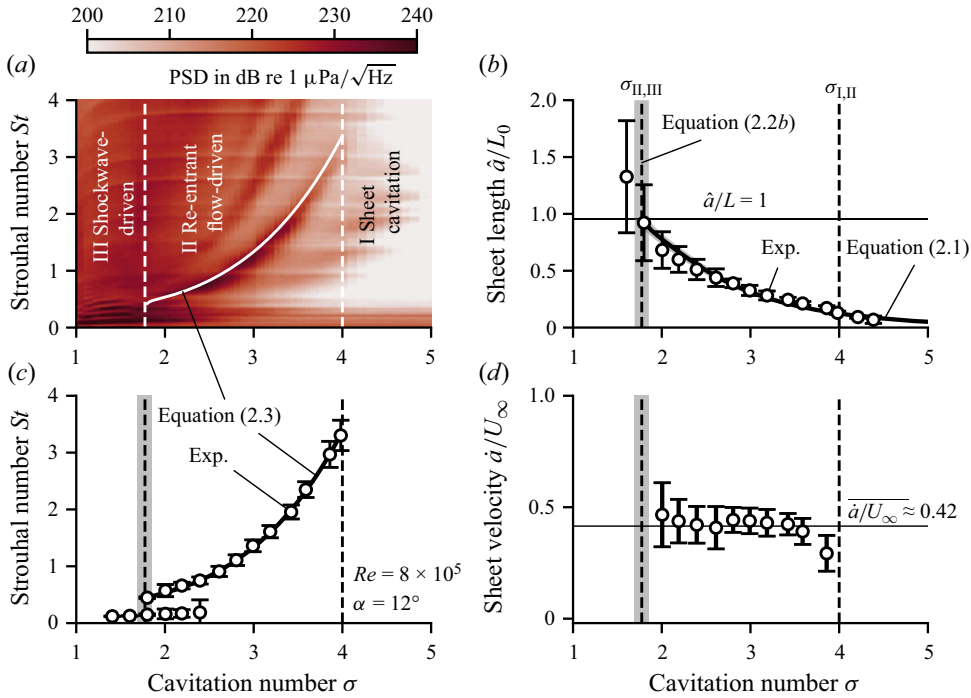


Figure 2. (a) Welch spectrogram of the hydrophone signal; (b) experimentally determined sheet length compared with the analytical model from (2.1); (c) Strouhal number vs cavitation number for the shockwave-driven and re-entrant flow-driven cloud cavitation. The dashed vertical lines represent the critical cavitation numbers  $\sigma_{II,III}$  and  $\sigma_{I,II}$ . The solid line is given by (2.3) with  $C = 0.42$  experimentally determined. (d) Sheet growth velocity. The Jupyter notebook for producing the figure can be found at [https://www.cambridge.org/S0022112024012242/JFM-Notebooks/files/figure\\_2/figure\\_2.ipynb](https://www.cambridge.org/S0022112024012242/JFM-Notebooks/files/figure_2/figure_2.ipynb).

attributed to the kinematic condition mentioned above, supported by the physical model and the experimental validation below.

Until now, shockwave-driven cloud cavitation, regime III, was described to be triggered by an abrupt stagnation in cavity growth. Ganesh (2015) came to this conclusion by the analysis of a nozzle flow which is not characterised by such a distinct typical length as is the case for the NACA 0015 hydrofoil with chord length  $L$  used in this study. Budich *et al.* (2018) carried out a numerical study for the same set-up and associate the initiation of the shock with the adverse pressure gradient. However, in the present study, there is a clear kinematic condition  $\hat{a} = L$  for the named transition. This hypothesis, in fact, is confirmed by the experimental model validation presented in this paper. The model is derived by predicting the sheet length  $\hat{a}$  from which the critical cavitation number,  $\sigma_{II,III}$ , is determined.

### 2.1. Critical cavitation number $\sigma_{II,III}$

The critical cavitation number  $\sigma_{II,III}$  defines the transition from re-entrant flow-driven cavitation (II) to shockwave-driven cavitation (III) for a lifting surface. When the condition  $\hat{a} = L$  is met, there is an abrupt stagnation of sheet growth, triggering a shockwave, and leading to a full extinction of the cavity sheet. From the asymptotic sheet length from (2.1),

and the condition  $\hat{a} = L$ , the critical cavitation number  $\sigma_{II,III}$  yields

$$c_p \left( \frac{\hat{a}}{L_0} = \frac{L}{L_0} \right) = 1.67 \left( \frac{f_0 R_0}{U_0} \right)^2 - \sigma_{II,III} \quad \text{or} \quad \sigma_{II,III} = c_p \left( \frac{L}{L_0} \right) - 1.67 \left( \frac{f_0 R_0}{U_0} \right)^2. \quad (2.2a,b)$$

Due to the Kutta condition, there is a stagnation point in irrotational flow at the trailing edge, i.e.  $c_p(1) = 1$ . However, from  $L/L_0 < 1$ , the discontinuous trailing edge and viscous calculation (Drela 1989) follows  $c_p(L/L_0) \neq 1$ .

The order of magnitude of the non-dimensionalised nucleation rate is  $(f_0 R_0 / U_0)^2 \sim 1$ , taking into account values for the nucleation rate,  $f_0 \sim 10^5$  Hz, the initial bubble radius,  $R_0 \sim 100 \mu\text{m}$ , and a typical velocity of  $U_0 \sim 10 \text{ m s}^{-1}$ . These values align with the numerical study conducted by Hsiao, Ma & Chahine (2017) and the experimental study by Pelz *et al.* (2017) and Groß & Pelz (2017).

Groß & Pelz (2017) conducted a study on diffusion-driven nucleation in a generic test rig, operating at high cavitation numbers. They deduced and validated that the nucleation frequency is proportional to the supersaturation of the liquid, gas solubility and the Weber and Péclet numbers to the powers of 3/4 and 1/3, respectively.

In the present study, alongside diffusion, evaporation also plays a role. A nucleation rate and an initial bubble size cannot be derived from experiments, since the physics of the nucleation mechanism at the cavity leading edge are considerably more complex, particularly for hydraulically smooth surfaces where instabilities, such as spanwise-moving cells, develop in the separated boundary layer, cf. Brandner *et al.* (2010) and Venning *et al.* (2022).

van Rijsbergen (2016) offers a thorough overview of potential nucleation mechanisms near the leading edge. In our study, we focus on the inception of surface-bound nuclei at high incidence angles. We conceptualise the nucleation mechanism as parallel streaks, initiating near the leading edge, although we recognise that the underlying physics are more complex, involving boundary layer effects and hydrodynamic instabilities, as detailed by Brandner *et al.* (2010). The dimensionless nucleation rate used here can be interpreted as a rate of vapour and air production. Despite being a coarse and simple model, the predicted sheet length shows good agreement with the results, as discussed in the context of external flows in this study and internal flows in the study by Pelz *et al.* (2017).

## 2.2. Strouhal number

In the following we derive an analytical model for the constant  $C$  being only dependent on the shape of the body;  $C$  is also known as the Strouhal number based on the asymptotic sheet length and has been experimentally found to be within 1/4 to 2/5 (Kawanami *et al.* 1997; Pham *et al.* 1999; Callenaere *et al.* 2001; Arndt 2012) and for three-dimensional hydrofoils approximately 1/5 (Foeth 2008).

The period of a shedding cycle  $\tilde{\tau} = 1/f$  in re-entrant flow-driven cloud cavitation is determined by the cumulative time needed for sheet growth  $\tilde{\tau}_s$  and the subsequent development of the re-entrant flow  $\tilde{\tau}_r$ :  $\tilde{\tau} = \tilde{\tau}_s + \tilde{\tau}_r$ . Non-dimensionalising the times by the advection time, i.e.  $\tau := \tilde{\tau} U_\infty / \hat{a}$ , and comparing with the dimensional analysis in § 2 yields

$$St := \frac{f L_0}{U_\infty} = \frac{1}{\tilde{\tau}} \frac{L_0}{U_\infty} = \frac{1}{\tilde{\tau}_s + \tilde{\tau}_r} \frac{L_0}{U_\infty} = \frac{1}{\tau_s + \tau_r} \frac{L_0}{\hat{a}} = C(\text{shape}) \frac{L_0}{\hat{a}}. \quad (2.3)$$

Thus, the shape constant reads  $C(\text{shape}) = 1/(\tau_s + \tau_r)$ . We now derive the non-dimensionalised times  $\tau_s$  and  $\tau_r$ . The time required for the cavity sheet to reach its

asymptotic value  $\hat{a}$  is  $\tilde{\tau}_s = \hat{a}/\dot{a}$  and thus  $\tau_s = U_\infty/\dot{a}$ , with  $\dot{a}$  being the average sheet growth velocity derived experimentally. The time needed for the re-entrant flow can be computed from the second-order nonlinear ordinary differential equation governing the re-entrant flow dynamics, see Pelz *et al.* (2017).

We solve the differential equation for the re-entrant flow coordinate  $\xi(t)$  which originates from the cavity closure against the flow direction, cf. figure 1. The initial conditions are  $\xi(0) = 0$  and  $\dot{\xi}(0) = U_0 = U_\infty\sqrt{1+\sigma}$ . Here,  $U_0$  is the initial re-entrant flow velocity from irrotational flow theory. Further, the height  $h_0$  of the re-entrant flow is required, usually being between 15% and 35% of the cavity sheet thickness (Callenaere *et al.* 2001). We determine  $h_0$  from the high-speed images as 15% of the cavity sheet thickness, cf. Pelz *et al.* (2017). Upon fulfilling the critical condition  $\xi/\hat{a} = 1$ , the re-entrant flow reaches the leading edge, which results in cloud shedding. This time instant is  $\tilde{\tau}_r$  and thus non-dimensionalised  $\tau_r = \tilde{\tau}_r U_\infty/\hat{a}$ . We should mention that we did not observe premature break-off, which occurs when the re-entrant flow penetrates the sheet before reaching the cavity leading edge, as described by Knapp (1955). Instead, the re-entrant flow reached the cavity leading edge, leading to cloud formation and shedding.

Even though the model is coarse, it predicts  $C$  well to be 0.34 for the given shape of the NACA 0015 hydrofoil, which is in the above-mentioned range known from experiments. The experimentally determined value reported in this paper, 0.42, is also of the same order of magnitude, cf. figure 2(c).

### 3. Experimental set-up

To validate the derived models, experiments were conducted in the high-speed water cavitation tunnel at the Chair of Fluid Systems, Technische Universität Darmstadt. The tunnel is a closed-loop circuit where the pressure can be varied from nearly vacuum up to 1600 kPa, cf. Hatzissawidis *et al.* (2021). Flow velocities up to  $U_\infty = 30 \text{ m s}^{-1}$  can be reached. The test section has a rectangular cross-sectional area with a height of 70 mm, a depth of 25 mm and a length of 462 mm. To ensure optical accessibility, the walls are made of acrylic glass. The NACA 0015 hydrofoil is made of stainless steel with a nominal chord length  $L_0$  and real chord length  $L$  of 46 mm and 44 mm, respectively. The blockage ratio in the test section at an incidence of  $12^\circ$  is 16.04%.

The fluid temperature is maintained at  $T = 23.5^\circ\text{C}$ . The free-stream velocity  $U_\infty$  in the test section is determined by measuring the volumetric flow rate using an ABB ProcessMaster500 FEP511-125D magnetic flow meter. It is kept constant at  $16.2 \text{ m s}^{-1}$  throughout the experiments with an uncertainty of 0.3% of the measured value. The oxygen content is determined by a VisiFerm DO Arc 120 H0 oxygen sensor and ranges from 4 to 8 ppm during the experiments.

The pressure  $p_\infty$  is measured using a Keller PAA-33X absolute pressure transducer with an uncertainty of 0.1% of full scale. Tunnel data were received using a National Instruments (NI) PCIe-6363 card at a sampling rate of 3000 Hz for 20 s. Measurement uncertainties were estimated according to ISO-GUM (ISO/TMBG Technical Management Board 2010).

During all the experiments, the Reynolds number was kept constant at  $8 \times 10^5$  and the hydrofoil was set at a fixed incidence  $\alpha$  of  $12^\circ$ . The cavitation number  $\sigma$  is varied from supercavitation,  $\sigma = 1$ , to no cavitation,  $\sigma = 5$ , covering the regimes I, II and III.

Simultaneous acoustic measurements and high-speed recordings with a dual-camera system were carried out to determine cavity sheet length  $\hat{a}$  and thickness  $h_0$ , and shedding frequencies as well as the power spectral density (PSD). A Brüel & Kjær (B&K) hydrophone type 8103 with a B&K conditioning amplifier type 2650 is flush mounted

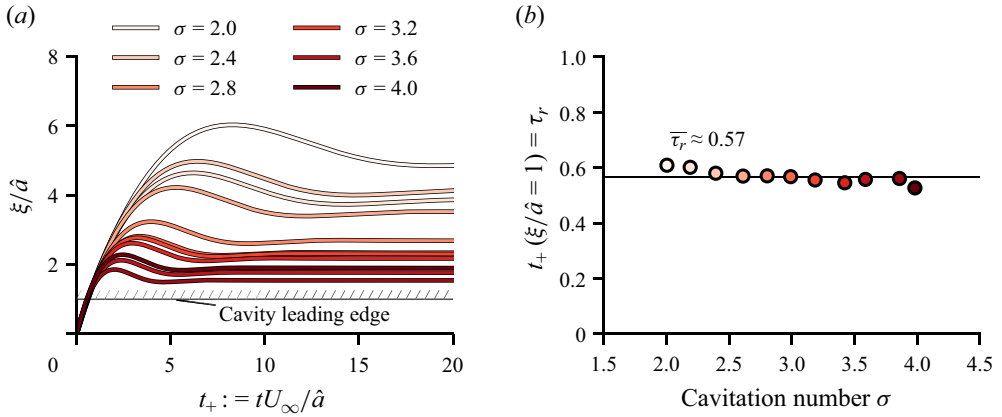


Figure 3. Re-entrant flow dynamics for cavitation numbers in the range between  $\sigma = 2$  and 4. (a) Solution of the differential equation in Pelz *et al.* (2017), (b) the time  $t_+$  when the re-entrant flow reaches the leading edge. The Jupyter notebook for producing the figure can be found at [https://www.cambridge.org/S0022112024012242/JFM-Notebooks/files/figure\\_3/figure\\_3.ipynb](https://www.cambridge.org/S0022112024012242/JFM-Notebooks/files/figure_3/figure_3.ipynb).

on the sidewall in a chamber. These data were recorded using a NI cDAQ-9189 chassis with a 16-bit NI 9223 voltage input module at a sampling rate of 200 kHz for a sampling time of 20 s to obtain clear spectra. The hydrophone signal is used similar to Smith *et al.* (2020) to calculate the PSD and generate a Welch spectrogram, figure 2(a), choosing a Hanning window with a window size of 20 000 or 0.1 s and an overlap of 50 %. The top and side views were recorded simultaneously to the acoustics by a Photron Fastcam Nova S12 operated at a frame rate of 18 000 fps with a spatial resolution of 0.078 mm px<sup>-1</sup> and an IDT MotionPro Y7 S3 operated at the same synchronised frame rate and a spatial resolution of 0.035 mm px<sup>-1</sup>, respectively. A total of 8001 frames were stored, resulting in a recording time of 0.45 s. Illumination was provided by two triggered Veritas Constellation 120 LED lights and one IDT 19-LED.

#### 4. Experimental validation and discussion

The Welch spectrogram, cf. figure 2(a), provides an overview of the cavitation regimes manifested throughout the variation of the cavitation number  $\sigma$ . Three regimes can be distinguished: I sheet cavitation, II re-entrant flow-driven cloud cavitation and III shockwave-driven cloud cavitation. The high-frequency shedding is correlated with II, wherein the frequency exhibits an increase with an increase in  $\sigma$  or a decrease in  $\hat{a}$ . Here, the low-frequency shedding is associated with III. The shedding frequency is independent of  $\sigma$ . An overlapping region of both frequency bands is evident from  $\sigma = 1.8$  up to 2.5.

We first compare the experimentally determined sheet length with the model from § 2.1. Based on the experimental data, the square of the non-dimensionalised nucleation rate  $(f_0 R_0/U_\infty)^2$  is determined to be 1.12 and supported by its 95 % confidence interval of  $\pm 0.05$ . This is of the same order of magnitude as derived in § 2.1. We achieve a good agreement for the asymptotic sheet length between the experiments and the analytical model, figure 2(b). The 95 % confidence interval of the asymptotic sheet length, represented by the grey-filled area in figure 3(b), is quantified through a Monte Carlo simulation that assumes a Gaussian distribution for the nucleation rate. The experimentally determined asymptotic sheet length is deduced from the top view of the high-speed imaging and the error bar represents the standard deviation across each cycle.



We can now anticipate the transition from re-entrant flow to shockwave-driven cloud cavitation. The critical cavitation number  $\sigma_{II,III}$  associated with the transition can be calculated from (2.2) as  $\sigma_{II,III} = 1.77$ , denoted by the dashed vertical line in figure 2(a–d). The 95 % confidence interval of the critical cavitation number  $\sigma_{II,III}$ , represented by the grey-filled area, is determined by a Monte Carlo simulation where the upper and lower bounds are 1.69 and 1.85, respectively. The prediction seems valid, since the high-frequency shedding associated with the re-entrant flow diminishes close to the predicted value, figure 2(a). A supplementary movie, available at <https://doi.org/10.1017/jfm.2024.1224>, shows the initiation of the shockwave for  $\sigma = 1.6$ . The shockwave speed in this movie is  $U_S/U_\infty \approx 0.83$ , which matches the values calculated by Bhatt *et al.* (2023) for the shockwave-driven cloud cavitation regime.

It should be clarified that, in the overlapping region,  $\sigma = 1.8$  to 2.5, both the high- and low-frequency bands, associated with re-entrant flow and condensation shockwaves, respectively, are evident. As the cavitation number decreases further, the low-frequency band intensifies, indicating that the shedding becomes more dominated by shockwaves rather than re-entrant flow. This observation aligns with the recent findings of Bhatt *et al.* (2023), which provide valuable insights into these complex and multimodal cloud cavitation mechanisms by introducing a probabilistic approach.

A new insight reported here is that, when the sheet reaches the trailing edge, there is a transition from re-entrant flow to shockwave. This transition is clearly visible in figure 2(a). Hence, the new findings are consistent with previous ones, but give a clearer picture of transient cloud cavitation.

Next, we determine the constant  $C$ , see § 2.2. From the experiment, the average time for the sheet to reach its maximum is  $\bar{\tau}_s = \overline{U_\infty/\hat{a}} \approx 2.38$ , cf. figure 2(d).

The re-entrant flow position  $\xi(t)/\hat{a}$  over the non-dimensionalised time  $t_+ := tU_\infty/\hat{a}$  is shown in figure 3(a), illustrating a growth pattern with a discernible peak before converging towards the asymptotic solution. An arrest of the re-entrant flow is experimentally reported by Venning *et al.* (2022), providing empirical support for the analytically derived kinematics.

It should be noted that, while the re-entrant flow momentum would theoretically be sufficient to extend upstream beyond the cavity leading edge, as indicated by  $\xi/\hat{a} > 1$ , this is not feasible in practice. Instead, when the re-entrant flow reaches the cavity leading edge, it triggers the formation of a cavitation cloud, which is then advected downstream.

The average time for the re-entrant flow to reach the cavity leading edge, i.e.  $\xi/\hat{a} = 1$ , is  $\bar{\tau}_r = 0.57$ , cf. figure 3(b). The mean velocity of the re-entrant flow is  $1.75U_\infty$ . Experimental findings by Pham *et al.* (1999) indicate re-entrant flow velocities ranging from 1.1 to 0.5 times the free-stream velocity, decreasing with distance from the cavity closure. Callenaere *et al.* (2001) and Gawandalkar & Poelma (2022) observed velocities around 0.5 of the velocity at the narrowest cross-section, corresponding to  $U_0$  in this study. We obtain for the average re-entrant flow velocity  $0.88U_0$ , being consistent with the values reported in the literature. However, the initial velocity is likely overestimated.

Substituting the average times  $\bar{\tau}_s = 2.38$  and  $\bar{\tau}_r = 0.57$  in (2.3) leads to  $St \approx 0.34L_0/\hat{a}$ . The value  $C = 0.34$  falls within the range of  $1/4$  and  $2/5$  reported in the literature. To compare this result with the experiments, we identify the Strouhal numbers of the fundamental modes from the high-speed imaging by applying spectral proper orthogonal decomposition, cf. Sieber, Paschereit & Oberleithner (2016), which provides us with the corresponding standard deviation, shown as error bars in figure 2(c). The identified Strouhal numbers match with the Welch spectrogram in figure 2(a). The constant  $C$  is determined from the experiments to be 0.42 through linear regression, which yields a high

coefficient of determination  $r^2 = 99.92\%$ , being larger than 0.34 as calculated from the model. This difference arises from the assumption that the whole cycle duration  $\tau$  is the sum of the time required for the sheet growth and the re-entrant flow development. In the experiments, the re-entrant flow already develops during sheet growth, leading to a higher Strouhal number, as predicted. Despite the simplicity of our model, the obtained value is reasonable.

## 5. Conclusions

The transition from re-entrant flow-driven to shockwave-driven cloud cavitation, as well as the determination of the Strouhal number for re-entrant flow-driven cavitation, were investigated for a NACA 0015 hydrofoil at a fixed Reynolds number and incidence, and varying cavitation number covering the regimes from shockwave-driven cloud cavitation (III), re-entrant flow-driven cloud cavitation (II) and sheet cavitation (I). High-speed imaging as well as high-frequency acoustic measurements using a hydrophone were conducted.

Regime II is associated with a high-frequency shedding which depends on the cavitation number, whereas regime III is associated with the low-frequency shedding independent of it. An overlapping region has been identified where both re-entrant flow and shockwave-driven cloud cavitation coexist, which aligns with the probabilistic approach presented in the recent study by Bhatt *et al.* (2023). As the cavitation number is reduced further, re-entrant flow-driven cavitation diminishes, and shockwave-driven cloud cavitation becomes the dominant mechanism. This transition occurs when  $\hat{a}/L = 1$ .

We derived the critical cavitation number  $\sigma_{II,III}$ , where the transition from regime III to II occurs, expanding our previous work on the transition from sheet to cloud cavitation (Pelz *et al.* 2017). Our experimental findings support the hypothesis, i.e.  $\hat{a}/L = 1$ ; the high-frequency shedding diminishes at approximately the predicted value  $\sigma_{II,III}$ . This offers a new understanding of the transition from re-entrant flow to shockwave-driven cloud cavitation for lifting surfaces, enabling more accurate predictions of this transition.

Despite the hypothesis suggesting that the abrupt stagnation of the sheet, cf. Ganesh (2015), or the adverse pressure gradient, cf. Budich *et al.* (2018), might trigger the shockwave, the discontinuous pressure distribution at the leading edge for a hydrofoil presents another mechanism to initiate the shockwave.

Next, the parameter  $C$  is derived to predict the Strouhal number  $St = CL_0/\hat{a}$ ;  $C$  is found to be 0.34, whereas 0.42 is estimated from a linear regression. Despite the simplicity of our model, the obtained value is reasonable and lies within the reported range: 1/4 and 2/5. This simple approach offers valuable new insights into the dynamics of the re-entrant flow, a key mechanism among the two principal drivers of cloud cavitation, facilitating a comprehensive understanding of its dynamic behaviour.

**Supplementary movie and Computational Notebook.** Supplementary movie and Computational Notebook files are available at <https://doi.org/10.1017/jfm.2024.1224>. Computational Notebooks can also be found online at <https://www.cambridge.org/S0022112024012242/JFM-Notebooks>.

**Acknowledgements.** The authors thank Mr U. Trometer and Mr A. Schuler for the technical support and manufacturing of the specimens.

**Funding.** The authors appreciate the support of the Federal Ministry for Economic Affairs and Climate Action (BMWK) on the basis of a decision by the German Bundestag (Grant number: 20395 N) and the Deutsche Forschungsgemeinschaft (German Research Foundation)–Project-ID 265191195–Collaborative Research Center 1194 (CRC 1194) ‘Interaction between Transport and Wetting Processes’, project C06.

**Declaration of interests.** The authors report no conflict of interest.

**Data availability statement.** The data and code are available in the JFM Notebook on <https://www.cambridge.org/S0022112024012242/JFM-Notebooks>. A supplementary movie is available.

**Author ORCIDs.**

 Grigorios Hatzissawidis <https://orcid.org/0000-0002-2073-0516>;

 Maximilian M.G. Kuhr <https://orcid.org/0000-0001-5676-4403>;

 Peter F. Pelz <https://orcid.org/0000-0002-0195-627X>.

**Author contributions.** G.H.: Conceptualisation, Methodology, Investigation, Validation, Formal analysis, Software, Data curation, Visualisation, Writing – original draft. M.M.G.K.: Project administration, Supervision, Writing – review & editing. P.F.P.: Conceptualisation, Funding acquisition, Supervision, Writing – review & editing.

REFERENCES

- ARNDT, R.E.A. 2012 Some remarks on hydrofoil cavitation. *J. Hydrodyn.* **24** (3), 305–314.
- ARNDT, R.E.A., SONG, C.C.S., KJELDSSEN, M., HE, J. & KELLER, A. 2000 Instability of partial cavitation: a numerical/experimental approach. In *Twenty-Third Symposium on Naval Hydrodynamics*. National Academies Press.
- BHATT, A., GANESH, H. & CECCIO, S.L. 2023 Partial cavity shedding on a hydrofoil resulting from re-entrant flow and bubbly shock waves. *J. Fluid Mech.* **957**, A28.
- BRANDNER, P.A., WALKER, G.J., NIEKAMP, P.N. & ANDERSON, B. 2010 An experimental investigation of cloud cavitation about a sphere. *J. Fluid Mech.* **656**, 147–176.
- BUDICH, B., SCHMIDT, S.J. & ADAMS, N.A. 2018 Numerical simulation and analysis of condensation shocks in cavitating flow. *J. Fluid Mech.* **838**, 759–813.
- CALLENAERE, M., FRANC, J.P., MICHEL, J.M. & RIONDET, M. 2001 The cavitation instability induced by the development of a re-entrant jet. *J. Fluid Mech.* **444**, 223–256.
- DE GRAAF, K.L., BRANDNER, P.A. & PEARCE, B.W. 2017 Spectral content of cloud cavitation about a sphere. *J. Fluid Mech.* **812**, R1.
- DE LANGE, D.F. & DE BRUIN, G.J. 1998 Sheet cavitation and cloud cavitation, re-entrant jet and three-dimensionality. *Appl. Sci. Res.* **58** (1–4), 91–114.
- DRELA, M. 1989 XFOIL: an analysis and design system for low Reynolds number airfoils. In *Low Reynolds Number Aerodynamics* (ed. T.J. Mueller), pp. 1–12. Springer.
- DULAR, M. & BACHERT, R. 2009 The issue of Strouhal number definition in cavitating flow. *J. Mech. Engng* **55** (11), 666–674.
- FOETH, E.-J. 2008 The structure of three-dimensional sheet cavitation. PhD thesis, Delft University of Technology.
- FURNESS, R.A. & HUTTON, S.P. 1975 Experimental and theoretical studies of two-dimensional fixed-type cavities. *Trans. ASME J. Fluids Engng* **97** (4), 515–521.
- GANESH, H. 2015 Bubbly shock propagation as a cause of sheet to cloud transition of partial cavitation and stationary cavitation bubbles forming on a delta wing vortex. PhD thesis, University of Michigan, Michigan.
- GANESH, H., MAKIHARJU, S.A. & CECCIO, S.L. 2016 Bubbly shock propagation as a mechanism for sheet-to-cloud transition of partial cavities. *J. Fluid Mech.* **802**, 37–78.
- GAWANDALKAR, U. & POELMA, C. 2022 The structure of near-wall re-entrant flow and its influence on cloud cavitation instability. *Exp. Fluids* **63** (5), 1–19.
- GROß, T.F. & PELZ, P.F. 2017 Diffusion-driven nucleation from surface nuclei in hydrodynamic cavitation. *J. Fluid Mech.* **830**, 138–164.
- HATZISSAWIDIS, G., LUDWIG, G.J. & PELZ, P.F. 2021 Modal decomposition of large- and small-scale cloud cavitation. *IOP Conf. Ser.: Earth Environ. Sci.* **774**, 012097.
- HSIAO, C.T., MA, J. & CHAHINE, G.L. 2017 Multiscale tow-phase flow modeling of sheet and cloud cavitation. *Intl J. Multiphase Flow* **90**, 102–117.
- ISO/TMBG TECHNICAL MANAGEMENT BOARD 2010 ISO/IEC Guide 98-3:2008.
- JAHANGIR, S., HOGENDOORN, W. & POELMA, C. 2018 Dynamics of partial cavitation in an axisymmetric converging-diverging nozzle. *Intl J. Multiphase Flow* **106**, 34–45.
- JAKOBSEN, J.K. 1964 On the mechanism of head breakdown in cavitating inducers. *Trans. ASME J. Basic Engng* **86** (2), 291–305.
- KAWANAMI, Y., KATO, H., YAMAGUCHI, H., TANIMURA, M. & TAGAYA, Y. 1997 Mechanism and control of cloud cavitation. *Trans. ASME J. Fluids Engng* **119** (4), 788–794.

- KJELDSEN, M., ARNDT, R.E.A. & EFFERTZ, M. 2000 Spectral characteristics of sheet/cloud cavitation. *Trans. ASME J. Fluids Engng* **122** (3), 481–487.
- KNAPP, R.T. 1955 Recent investigations of the mechanics of cavitation and cavitation damage. *Trans. ASME J. Fluids Engng* **77** (7), 1045–1054.
- LE, Q., FRANC, J.P. & MICHEL, J.M. 1993 Partial cavities: global behavior and mean pressure distribution. *Trans. ASME J. Fluids Engng* **115** (2), 243–248.
- LEROUX, J.B., COUTIER-DELGOSHA, O. & ASTOLFI, J.A. 2005 A joint experimental and numerical study of mechanisms associated to instability of partial cavitation on two-dimensional hydrofoil. *Phys. Fluids* **17** (5), 052101.
- LUSH, P.A. & SKIPP, S.R. 1986 High speed cine observations of cavitating flow in a duct. *Intl J. Heat Fluid Flow* **7** (4), 283–290.
- PELZ, P.F., KEIL, T. & GROSS, T.F. 2017 The transition from sheet to cloud cavitation. *J. Fluid Mech.* **817**, 439–454.
- PHAM, T.M., LARRARTE, F. & FRUMAN, D.H. 1999 Investigation of unsteady sheet cavitation and cloud cavitation mechanisms. *Trans. ASME J. Fluids Engng* **121** (2), 289–296.
- REISMAN, G.E., WANG, Y.C. & BRENNEN, C.E. 1998 Observations of shock waves in cloud cavitation. *J. Fluid Mech.* **355**, 255–283.
- VAN RIJSBERGEN, M. 2016 A review of sheet cavitation inception mechanisms. In *16th International Symposium on Transport Phenomena and Dynamics of Rotating Machinery*.
- SIEBER, M., PASCHEREIT, C.O. & OBERLEITHNER, K. 2016 Spectral proper orthogonal decomposition. *J. Fluid Mech.* **792**, 798–828.
- SMITH, S.M., VENNING, J.A., PEARCE, B.W., YOUNG, Y.L. & BRANDNER, P.A. 2020 The influence of fluid–structure interaction on cloud cavitation about a stiff hydrofoil. Part 1. *J. Fluid Mech.* **896**, A1.
- TRUMMLER, T., SCHMIDT, S.J. & ADAMS, N.A. 2020 Investigation of condensation shocks and re-entrant jet dynamics in a cavitating nozzle flow by large-eddy simulation. *Intl J. Multiphase Flow* **125**, 103215.
- VENNING, J.A., PEARCE, B.W. & BRANDNER, P.A. 2022 Nucleation effects on cloud cavitation about a hydrofoil. *J. Fluid Mech.* **947**, A1.
- WU, J., GANESH, H. & CECCIO, S. 2019 Multimodal partial cavity shedding on a two-dimensional hydrofoil and its relation to the presence of bubbly shocks. *Exp. Fluids* **60** (4), 1–17.
- WU, X., MAHEUX, E. & CHAHINE, G.L. 2017 An experimental study of sheet to cloud cavitation. *Exp. Therm. Fluid Sci.* **83**, 129–140.
- ZHANG, G., ZHANG, D., GE, M., PETKOVŠEK, M. & COUTIER-DELGOSHA, O. 2022 Experimental investigation of three distinct mechanisms for the transition from sheet to cloud cavitation. *Intl J. Heat Mass Transfer* **197**, 123372.